



Extremely suppressed thermal conductivity of large-scale nanocrystalline silicon through inhomogeneous internal strain engineering

Journal:	<i>Journal of Materials Chemistry A</i>
Manuscript ID	TA-ART-05-2023-003011.R1
Article Type:	Paper
Date Submitted by the Author:	05-Aug-2023
Complete List of Authors:	Xu, Bin; University of Tokyo Liao, Yuxuan; University of Tokyo Fang, Zhenglong; University of Tokyo Li, Yifei; University of Tokyo Guo, Rulei; University of Tokyo Nagahiro, Ryohei; University of Tokyo Ikoma, Yoshifumi; Kyushu University Kohno, Masamichi ; Kyushu University, Shiomi, Junichiro; University of Tokyo,

ARTICLE

Extremely suppressed thermal conductivity of large-scale nanocrystalline silicon through inhomogeneous internal strain engineering

Received 00th January 20xx,
Accepted 00th January 20xx

DOI: 10.1039/x0xx00000x

Bin Xu^{a,b}, Yuxuan Liao^a, Zhenglong Fang^a, Yifei Li^a, Rulei Guo^a, Ryohei Nagahiro^a, Yoshifumi Ikoma^c, Masamichi Kohno^{d,e}, Junichiro Shiomi^{a,b*}

Reducing the lattice thermal conductivity (κ_L) of dense solid materials is critical for thermal insulation and thermoelectrics. Although nanocrystalline materials formed on a large-scale by hot pressing or sintering nanoparticles can achieve low κ_L , there is still considerable room for further reduction. In this study, a moderate high-pressure torsion (HPT) process is applied on nanocrystalline silicon to further reduce the κ_L by directly introducing finer nanostructures and internal strain without causing phase transition. Unlike conventional approaches that manipulate the phonon mean free path through the classical "size effect", the inhomogeneous internal strain induced by HPT leads to overall lattice softening and a significant boundary softening effect, which can reduce the phonon group velocity, and enhance the phonon scattering at grain boundaries, respectively. This can thereby bring extra suppression on κ_L , achieving a record low κ_L of 1.49 W/m-K for being a fully dense bulk silicon without any amorphous or metastable phases, which is comparable to its amorphous counterpart. This study demonstrates a practical and feasible strain engineering strategy for realizing low κ_L that is applicable to various nanocrystalline materials.

Introduction

Phonon engineering has made significant advances in recent years, thereby enabling the manipulation of phonon propagation and tuning of the lattice thermal conductivity (κ_L) of solid materials. These advancements have facilitated the development of materials with both high and low κ_L to meet the rapidly increasing demands for thermal dissipation, thermal insulation, and thermoelectrics. When developing crystalline materials with lower κ_L , a key issue is modulating the state or kinetics of phonons to reduce the characteristic group velocities and lengths of transport.

A popular, effective approach in reducing κ_L is nanostructuring. Fabricating nanostructures with a characteristic distance between the interface smaller than the intrinsic phonon mean free path (MFP) can effectively scatter phonons and reduce the MFP. This has been demonstrated for various types of nanostructures, such as nanoinclusions^{1,2}, grain boundaries³,

and hierarchical nanostructures⁴. Modulating phonon states with nanostructures smaller than the phonon coherence length has also been demonstrated. The interference of phonon waves reflected at different interfaces modulates the phonon dispersion relations, thereby decreasing the group velocity and enabling the formation of band gaps. Such heat conduction manipulation by phonon coherence has been reported for various nanostructures, including superlattices⁵⁻⁷, phononic crystals^{8,9}, and 2D van der Waals heterostructures¹⁰. Further, κ_L can also be reduced by enhancement of lattice anharmonicity and crystal complexity^{11,12}. Theoretical calculations have shown that disorder scattering and force-field inhomogeneity can concurrently reduce phonon group velocity and MFP in alloying materials, such as $\text{In}_{1-x}\text{Ga}_x\text{As}$ ¹³ and $\text{PbTe}_{1-x}\text{Se}_x$ ¹⁴.

As large-scale materials are important for practical applications, numerous studies on bulk nanocrystalline materials with low κ_L , typically fabricated by hot pressing or sintering nanoparticles, have been conducted^{1,4,15-17}. Among them, nanocrystalline silicon has been widely studied because of its high abundance and potential for use in thermoelectrics¹⁸. Additionally, it has served as a representative case that can benefit from nanostructuring because of the high intrinsic κ_L . Bulk nanocrystalline silicon fabricated by nanoparticles with sizes of 10–15 nm have achieved low κ_L at room temperature, varying from 4.7 to 24.3 W/m-K with average grain sizes ranging from 25 to 100 nm¹⁹⁻²³. Among them, the lowest reported κ_L at room temperature thus far is approximately 4.7 W/m-K, which was obtained for an average grain size of 32 nm²¹. Theoretically, a lower κ_L can be obtained by decreasing the grain size;

^a Department of Mechanical Engineering, The University of Tokyo, 7-3-1 Hongo, Bunkyo, Tokyo 113-8656, Japan. E-mail: shiomi@photon.t.u-tokyo.ac.jp

^b Institute of Engineering Innovation, The University of Tokyo, 2-11 Yayoi, Bunkyo, Tokyo 113-8656, Japan

^c Department of Materials Science and Engineering, Kyushu University, 744 Motoooka, Nishi-ku, Fukuoka, 819-0395, Japan

^d Department of Mechanical Engineering, Kyushu University, 744 Motoooka, Nishi-ku, Fukuoka 819-0395, Japan

^e International Institute for Carbon-Neutral Energy Research (WPI-I2CNER), Kyushu University, 744 Motoooka, Nishi-ku, Fukuoka 819-0395, Japan

Electronic Supplementary Information (ESI) available: [details of any supplementary information available should be included here]. See DOI: 10.1039/x0xx00000x

Table 1. Properties of HPT samples

Sample ID	Thermal conductivity (W/m-K)	Density (g/m ³)	relative density	Grain size from XRD (nm)	Grain size from EBSD (nm)	Mean internal strain $C\epsilon$	Sound velocity vs (m/s)
As-sintering	2.1~2.7	1.59~1.63	0.679	53.8	84.3 (± 19.3)	0.00661	3910
0 rotation	3.80	2.2902	0.990	36.5	31.4 (± 22.9)	0.0195	3692
1/4 rotation	1.64	2.3391	1.011	33.9	28.8 (± 9.3)	0.0249	3040
1/2 rotation	1.49	2.3097	0.998	32.4	28.2 (± 8.6)	0.0252	2856

however, this would require starting from very small nanoparticles and preventing grain growth during high temperature processes, such as hot pressing or sintering. Therefore, a non-heating post-treatment process that can introduce a finer nanostructure directly into bulk nanocrystalline materials is highly valuable. Consequently, the high-pressure torsion (HPT) method is a viable option. The HPT method can apply considerable pressure and torsion^{24,25} throughout materials in a scalable manner, thus leading to the formation of and variation in nanostructures without heating the materials²⁶.

Previous studies have reported the effect of HPT in inhibiting the κ_L of silicon. Harish et al. used HPT to reduce the κ_L of single-crystal silicon from 150 to 7.6 W/m-K because of the decrease in grain size caused by plastic deformation²⁷. Shao et al. analyzed the decreasing κ_L in a similar HPT process by

combining density functional theory (DFT) calculation, Monte Carlo ray-tracing method, and effective medium theory analysis²⁸. They reported that the enhancement in phonon boundary scattering due to the decrease in grain size and generation of low thermal conductive metastable phases of silicon, such as body-centered cubic BC8 (Si-III) and rhombohedral R8 (Si-XII) phases, are responsible for the reduced κ_L . By adjusting the HPT parameters, the generation of metastable phases and the grain refinement can be further controlled, which achieved a more significantly suppressed thermal conductivity of 3 W/m-K²⁹. Although previous studies have applied the HPT process to single-crystal silicon to produce nanocrystals with a metastable phase, HPT has not yet been applied to nanocrystalline silicon to modulate existing nanograins and interfaces.

Considering another perspective, during HPT, the enormous strain/stress introduced to the lattice during the process should directly influence κ_L . Suppression of κ_L due to lattice strain has been widely studied for various materials and approaches. Kodama et al. realized a stress-induced κ_L suppression of 35–55 % by encapsulating fullerene inside carbon nanotubes³⁰. Biswas et al. realized a strain-induced κ_L suppression of approximately 35 % by arranging small volume fractions of SrTe into PbTe³¹. For silicon, theoretical calculations on single crystal silicon/silicon nanowires have proven the ability of strain to reduce κ_L ³². Experimental studies on silicon thin-films with periodic punching holes have also shown strain-induced lattice softening and the resulting reduced κ_L ³³. Therefore, by combining the effects of grain size reduction and strain introduction, HPT processing is promising for the ultimate suppression of κ_L . In the previous studies that applied HPT on single crystal silicon with larger pressure and degree of rotation to generate metastable phase³⁴, the observed strain was minor, presumably due to structural relaxation upon the phase transition. In this regard, a crucial aspect lies in preventing the transition to a meta-stable phase by moderating the applied pressure and torsion.

This study aimed to achieve suppression of κ_L of large-scale nanocrystalline silicon using an HPT process. To realize strain engineering, HPT was performed without generating metastable and amorphous phases by adopting moderate pressure and torsion. Further, systematic structure characterization and theoretical calculations were performed to understand the underlying mechanism and determine the vital role of inhomogeneous internal strain and grain size reduction in reducing thermal conduction.

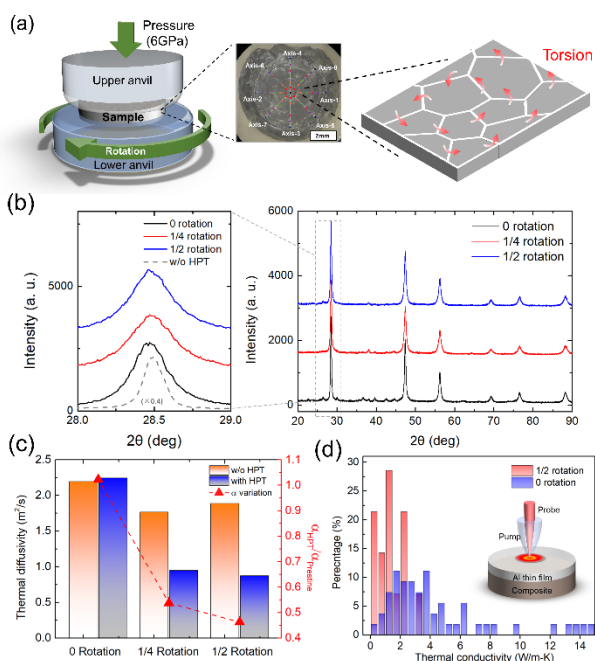


Figure 1. Thermal conductivity and structural evolution of silicon crystals by HPT processing. (a) Schematic of HPT instrument and method; inset is the picture of the as-processed sample and a schematic of how the stress is introduced. (b) XRD spectrum of the HPT samples with different rotations. The inset is the magnified region near $2\theta = 28.5$; the grey spectrum is the XRD spectrum before the HPT process, and its intensity is reduced by 0.4 times. (c) Thermal diffusivity of samples before ($\partial_{Prestine}$) and after the HPT process (∂_{HPT}) with different degree of rotations and the corresponding variation rate ($\partial_{HPT}/\partial_{Prestine}$) measured by the laser flash method. (d) Thermal conductivity distribution of 0 and 1/2 rotation samples measured by the TDTR method; inset is the schematic of the sample structure for TDTR measurement.

Experimental methods

Sample fabrication

the 2θ peaks at 28.5° , 47.5° , 56.2° , 69.3° , 76.6° , and 83.3° , all originating from diamond cubic phase silicon. Additionally, the

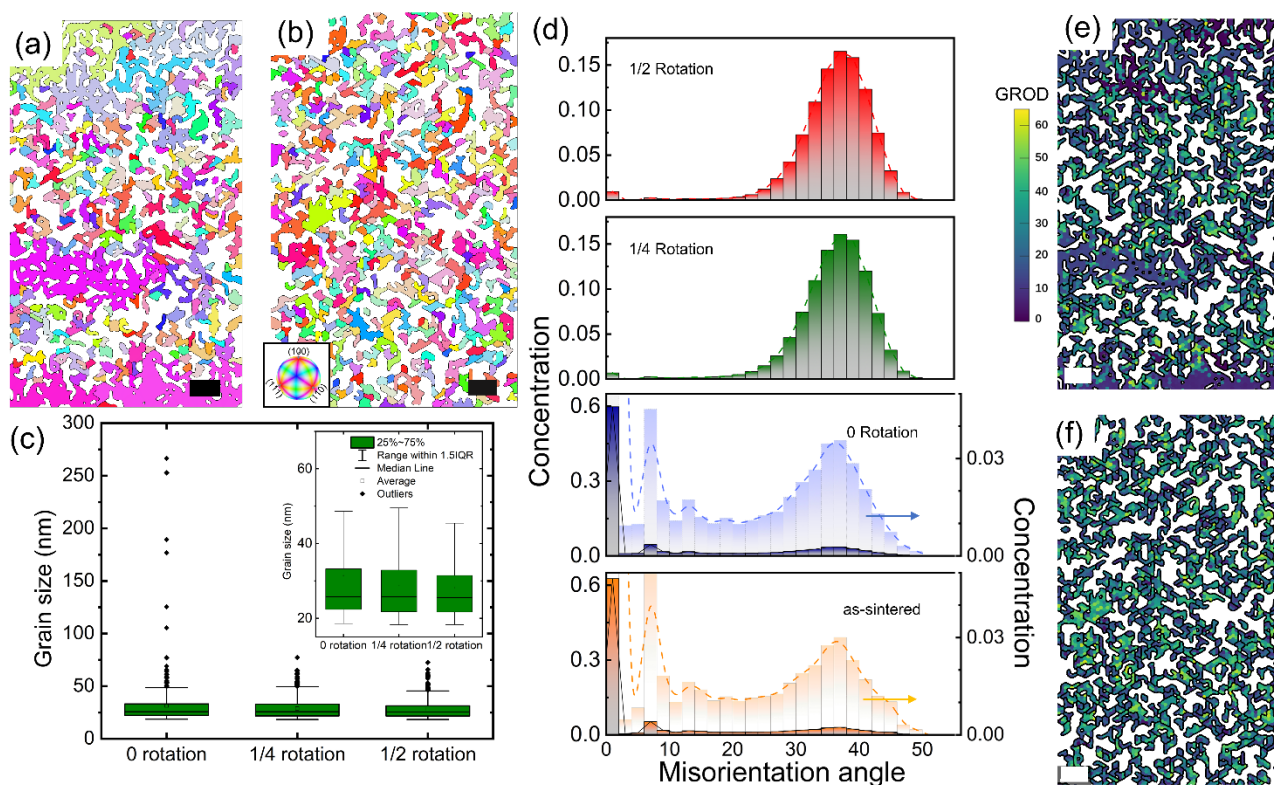


Figure 2. EBSD analysis of the nanostructure of HPT sample. KAM mapping of HPT samples processed under (a) 0 rotation and (b) 1/2 rotation. (c) Grain size distribution of 0–1/2 rotation HPT samples. (d) Distribution of misorientation angle of as-sintered silicon and silicon processed by HPT with rotations from 0 to 1/2. GROD mapping of (e) 0- and (f) 1/2-rotation HPT sample. Note, the scalebar in (a), (b), (e), (f) is 75 nm.

HPT processing was employed for a silicon nanocomposite that was initially fabricated by plasma sintering under identical conditions. In the sintering process, silicon nanoparticles with the addition of 0.5 wt% of silver nanoparticles were used following our previous work³⁵ (Details in SI: Methods). Note here that the small amount of silver nanoparticles has a negligible effect on the thermal conductivity, as shown by the scattering rate analysis (Details in SI).

Three nanocrystal bulk silicon samples with similar thermal diffusivities (within $1.77\text{--}2.19\text{ m}^2/\text{s}$) were used, and the average grain size was approximately 55 nm according to the X-ray diffraction (XRD) analysis. The HPT process involved applying a pressure of 6 GPa and gradually increasing the rotation angle, as shown in the schematic in Fig. 1(a). To avoid the formation of metastable phases, such as the body-centered cubic BC8 (Si-III) and rhombohedral R8 (Si-XII) phases²⁸, the pressure was set lower than that used in a typical HPT process (~ 20 GPa), and the rotation was limited to 0, 1/4, and 1/2 (samples #1–#3), which is less than the typically used 5–20 rotations. Herein, the values 0, 1/4, and 1/2 represent the degree of rotation of the lower anvil, where 1/4 and 1/2 mean that the lower anvil was rotated by 90 and 180 degrees, respectively.

XRD measurements were performed to characterize the configuration variation (Fig. 1(b)); the XRD analysis revealed the absence of metastable phases in HPT samples (Fig. 3(a)), with

absence of the amorphous silicon baseline in the XRD spectrum indicated a negligible component of the amorphous phase. Furthermore, an evident broadening of the silicon XRD peaks was observed (inset of Fig. 1(b)). Note here, the two secondary peaks at 26.4° and 38.1° with small intensity do not originate from the metastable phase of silicon. They are from the graphite on the sample surface due to contact with graphite die and electrode during the sintering and the small amount of silver nanoparticles (approximately 0.5 wt%), which have negligible effects on the thermal conductivity (details discussed in SI).

This variation indicates either a reduction in nanocrystal size or generation of internal strain, which is discussed later.

Thermal conductivity measurement

The thermal diffusivity of the HPT samples was measured by the laser flash method (details in SI: Method). The thermal diffusivity remained almost unchanged when only compression was applied; however, when rotation was introduced, the thermal diffusivity dropped to 55 % and 46 % for 1/4 and 1/2 rotation, respectively (Fig. 1(c)). As measured by the Archimedes method, the HPT process also led to a relative density of approximately 100 % due to destruction of the porous structure in the as-sintered sample (Table 1.). This allowed us to calculate κ_L using the theoretical value of heat capacity. Impressively, the κ_L of the 1/2 rotation sample

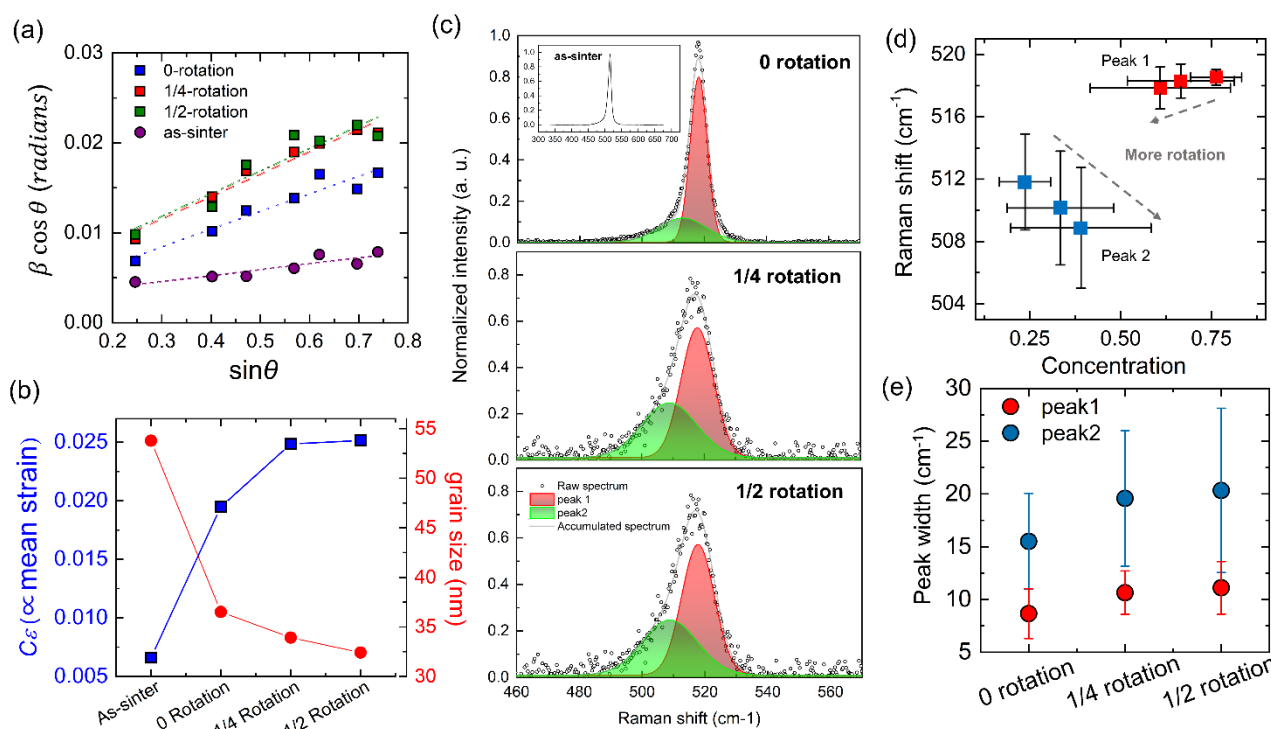


Fig. 3 Internal inhomogeneous strain characterization of as-sintered and HPT processed silicon under 0–1/2 rotation. (a) Williamson–Hall plot, and (b) grain size and mean strain ($C\epsilon$) obtained from the analysis. (c) Representative Raman spectrum and the two predominate components obtained from Voigt function fitting. (d) Raman shift, peaks concentration, and (e) peak width variation in the two subcomponents shown in (c). Data are collected from more than 30 measurements at different locations.

dropped to 1.49 W/m-K, which is comparable to that of amorphous silicon ($\kappa_L = 1.5$ W/m-K). This is rare for a 100 % dense bulk-scale silicon crystal and suggests that HPT is a valuable tool for achieving low κ_L . Herein, given our primary objective to modify the lattice thermal conductivity, we intentionally avoided carrier doping and sought to mitigate its corresponding influence on thermal conductivity. This can dramatically simplify our analysis of lattice thermal conductivity. To ensure the thermal conductivity contribution from the charge carrier is negligible, we verified the electronic thermal conductivity via the Wiedemann-Franz law, utilizing our experimentally measured electrical conductivity. We found this to be roughly three orders of magnitude smaller than the lattice thermal conductivity (Details in SI).

Additionally, local thermal conductivity was measured using the time-domain thermoreflectance (TDTR) method to further investigate the variation in κ_L distribution. Figure 1(d) shows the histogram of the local thermal conductivity distribution for the 0 and 1/2 rotation samples, which were taken from randomly chosen positions (details in SI: Methods). The κ_L distribution became narrower when rotation was applied, and the average values decreased. This reduction in the average κ_L is consistent with the results of laser flash. In addition, the narrowing of the κ_L distribution suggests that a more uniform structure was generated.

Results and discussion

Structural characterization

To explain the variation in κ_L and its distribution, a nanoscale perspective on the morphology variation is necessary. To this end, electron backscatter diffraction pattern (EBSD) measurements were performed to trace the nanocrystal structure variation under the HPT process. Figures 2 (a) and (b) show the kernel average misorientation (KAM) mapping of the 0 and 1/2 rotation samples, respectively, thereby revealing the local grain misorientation and the grain size. The misorientation angle in the KAM mapping can quantify the local misorientation between neighbouring grains, which reflects the grain orientation randomness and the amount of misalignment or lattice distortion at the grain boundary. After applying rotation, the component of relatively large grains exceeding 100 nm was eliminated (black dots enclosed in grey dash line; Fig. 2(c)). Simultaneously, an evident decrease in grain size occurred for small crystals, thus resulting in a slight decrease in the average grain size and dominant grain size distribution range. Furthermore, the components with relatively small misorientation angles (0–15°) in both as-sintered and 0 rotation samples disappeared after the rotation process (more EBSD results are provided in Figs. S1 and S2). The simultaneous disappearance of the low misorientation angle and the large grains indicates a possible structure variation; essentially, new grain boundaries were created from large grains and subsequently underwent fragmentation and continuous deformation, which turned them into new grains that are much more disordered and tortuous. Consequently, nanocrystal structures with relatively uniform grain size and inhomogeneous crystal orientation were generated, owing to

which the κ_L distribution became narrower in the microscale spatial resolved TDTR measurement.

Moreover, the grain reference orientation deviation (GROD) mapping (Figs. 2 (e) and (f)), which reflects the lattice misfit inside individual nanograins, indicates an increase in internal inhomogeneous strain inside individual grains. A similar conclusion can be drawn from the result of the Williamson–Hall analysis³⁶ (details of the Williamson–Hall analysis are provided in SI: Methods). By fitting the peak broadening (β_{total}) of XRD data with the equation $\beta_{total} \cos \theta = C\varepsilon \sin \theta + K\lambda/D$, the corresponding internal strain from the slope ($C\varepsilon$) and the grain size information can be obtained from the intercept ($K\lambda/L$) (Fig. 3 (a)). The internal strain term $C\varepsilon$ increased significantly after applying pressure and gradually increasing the rotation angle in sequence. Simultaneously, the average grain size reduced from 54 to 36.5 nm and then further decreased to 32.5 nm. The trend and absolute magnitude of average grain size agree with the EBSD analysis results. Note that $C\varepsilon$ reflects only the relative change in the inhomogeneous internal strain, whereas the absolute magnitude depends on the C value, which varies between different materials. By contrast, the peak position in the XRD spectrum (Fig. 1(b)) shifted slightly downward ($\Delta 2\theta = 0.03^\circ$), thus indicating that the homogeneous tensile strain of the entire sample was negligibly small (approximates 0.1 % of tensile strain).

Raman spectroscopy was employed to quantitatively identify the internal strain. Fig. 3 (c) displays the representative Raman spectrum of 0, 1/4, and 1/2 rotation samples. As the rotation increased from 0 to 1/2, a significant downshift and peak broadening occurred for the 520.5 cm^{-1} peak. Along with the peak broadening, the peak became asymmetric with an increase in the minor component at low wavenumbers. In comparison, the 520 cm^{-1} peak of the as-sintered sample was highly symmetric (inset of Fig. 3(c)). A Voigt profile function was used in fitting the Raman spectrum to obtain the Raman shift

and the concentration of individual peak components at high (peak 1) and low (peak 2) wavenumbers (Fig. 3(a)). To ensure the accuracy of the results, more than 30 data points were evenly taken on the sample, as depicted in Fig 1(a). When the rotation was increased from 0 to 1/2, peak 1 exhibited a downshift from 518.5 to 517.8 cm^{-1} , and peak 2 exhibited a more remarkable downshift from 511.8 to 508.9 cm^{-1} (Fig. 3 (d)). The downshift in the Raman peaks suggests the presence of tensile stress inside the sample. The average internal stress for the major component of peak 1 can be calculated using the shift in Raman peaks, following the relation: 1 cm^{-1} in Raman shift represents 0.5 GPa stress^{37,38}. The results indicate that the tensile stress increased from 0.51 to 1.09 GPa after 1/4 rotation and reached 1.34 GPa after 1/2 rotation. For peak 2, the above relationship is not applicable for obtaining the magnitude of the stress owing to the overly large downshift (details in SI: Methods). Nevertheless, the significant downshift indicates that the stress in the peak 2 component is much more substantial than that observed in peak 1. Moreover, the normalized proportion of peak 2 to the overall intensity of peak 1 and 2 increased from 0 to 23.6 % under 0 rotation, and then increased to 39 % under 1/2 rotation. (Fig. 3(d)). As the EBSD measurement elucidated that the decrease in grain size by HPT rotation occurs from the interface and residual internal stress concentrates in the defective or interfacial parts of a polycrystal, the interfacial layer contributes to the peak 2 components^{39,40} because it experiences a higher degree of deformation during HPT processing compared with the bulk grains. This result indicates an increase in the interfacial layer thickness occurs during the HPT processing, reflecting the enhancement of the strain concentrated at the interface. Furthermore, under such a process, the peak width of individual Raman peaks also increases, thus indicating an increase in structural inhomogeneity both inside the grains and in the interfacial layer.

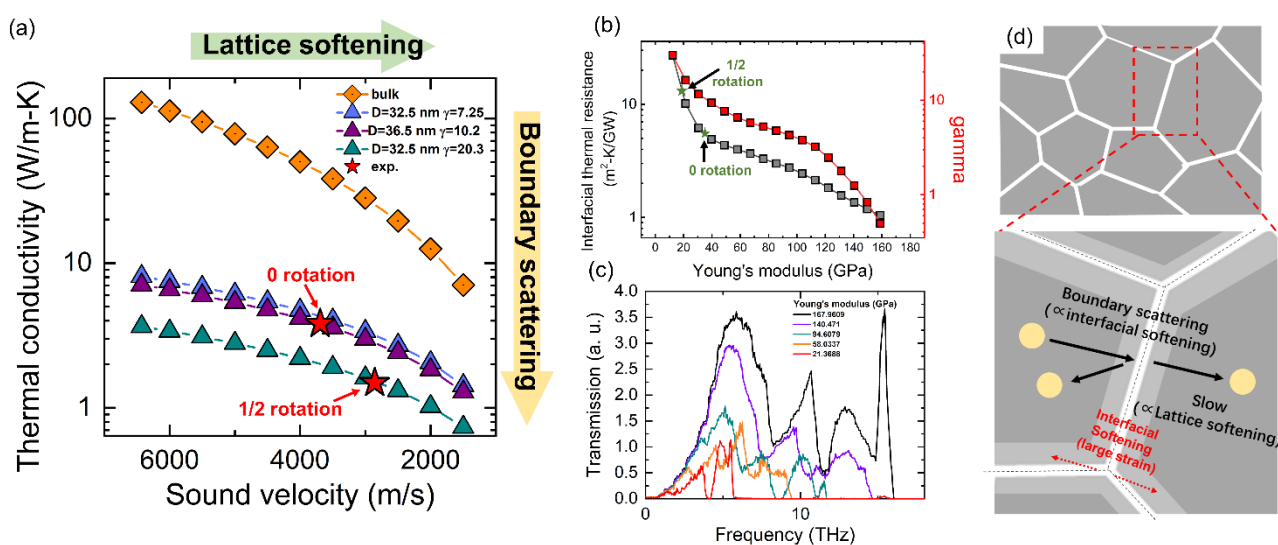


Fig. 4 Theoretical analysis of the mechanism responsible for the low thermal conductivity. (a) Theoretical thermal conductivity under different sound velocities and interfacial thermal resistance as evaluated by index γ . (b) interfacial thermal resistance, γ , and (c) the interfacial phonon transmission spectrum obtained from the AGF calculation performed under different interfacial softening conditions (interfacial layer thickness, 5 nm); the experimental data of the 0 and 1/2 rotation sample correspond to the left axis. (d) Structure evolution and the corresponding effect on phonon transport responsible for the low thermal conductivity.

Internal strain inhomogeneity can strongly impact phonon transport, as reflected by the decrease in acoustic velocity (details of acoustic velocity measurement are in SI: Methods). Herein, we measured both the longitude (v_L) and transverse (v_T) acoustic velocity, and calculated the sound velocity (v_S) by:

$$v_S = \left(\frac{1}{3} \left[\frac{1}{v_L^2} + \frac{2}{v_T^2} \right] \right)^{-\frac{1}{2}} \quad (1)$$

When pressure was applied, the sound velocity decreased from 3911 to 3693 m/s and continued to decrease with more significant torsion. In the 1/2 rotation sample, the sound velocity reached 2857 m/s, corresponding to a 27 % reduction compared with the as-sintered silicon nanocrystal. This is even less than 45 % of that of single-crystal silicon (6428 m/s; Table 1).

Thermal conductivity model and discussion

A theoretical calculation was performed to include the impact of all the abovementioned configuration variations on κ_L . κ_L is understood in terms of various lattice vibrational modes and is expressed as:

$$\kappa_L = \frac{1}{3} \sum_s \int_0^{\omega_{max}} C(\omega, s) \tau(\omega, s) v_g^2(\omega, s) d\omega \quad (2)$$

where C , v_g , τ , s , and ω are heat capacity, phonon group velocity, relaxation time, phonon branch, and phonon frequency, respectively. The phonon boundary scattering term was included in the total relaxation time (τ_{total}) based on Matthiessen's rule (equation 3) to account for the effect of strain and nanograin size variation on κ_L , as follows.

$$1/\tau_{total} = 1/\tau_{pp} + 1/\tau_{bd} \quad (3)$$

where the subscript pp and bd are intrinsic phonon–phonon and phonon–boundary scatterings, respectively. The boundary scattering term τ_{bd} is expressed as⁴¹:

$$\tau_{bd}^{-1} = v_g \left[\left(\frac{3}{4} \frac{t}{1-t} D \right)^{-1} + (1.12D)^{-1} \right]^{-1} \quad (4)$$

$$t = 1/(1 + \gamma\omega/\omega_{Max}) \quad (5)$$

where t is the phonon transmittance at grain boundaries; ω_{Max} is the cutoff phonon frequency; D is the grain size; and γ is a term related to interfacial thermal resistance, which can be obtained from the interfacial phonon transmission spectrum⁴² (Fig. 4 (b)). Next, to consider the influence of strain, τ_{pp} was calibrated by the measured sound velocity v_S , following the equation proposed in a previous study⁴³.

$$\frac{1}{\tau_{pp}} = \frac{c_1 \omega^2 T}{v_s^3} e^{-c_2 v_s/T} \quad (6)$$

where T is the temperature; and c_1 and c_2 are expressed as $c_1 = v_s^3 C_1$ and $c_2 = C_2/v_s$, respectively, where C_1 and C_2 are constants obtained from ref.⁴⁴. Moreover, the group velocity term under a particular strain was calibrated using $v_g/v_{g0} = v_S/v_{S0}$, where the subscripts $g0$ and $s0$ represent the phonon group velocity and sound velocity under zero strain, respectively. Using the phonon properties of zero-strain silicon

obtained from the first-principles-based anharmonic lattice dynamics⁴⁵, κ_L was calculated under different grain sizes and interfacial transmission conditions as a function of the sound velocity (Fig. 4 (a)). This result can assess the relative contributions of lattice softening and phonon–boundary scattering on κ_L under different grain sizes and interfacial transmission conditions. With the decrease in sound velocity (lattice stiffness), the κ_L was remarkably suppressed. For single-crystal silicon, the decrease in κ_L as a function of sound velocity exhibits an approximate cubic trend. This is because κ_L is proportional to v_g^3 as its expression can be transformed into:

$$\kappa_L = \frac{(6\pi^2)^{2/3} \bar{M} (v_g^3)}{V^{2/3} 4\pi\gamma^2 T} = A \frac{v_S^3}{T} \quad (7)$$

when the phonon–phonon scattering becomes predominate in single crystal ($\tau_{pp} = \tau_{total}$)⁴³. When considering the boundary scattering, κ_L is further suppressed under either smaller grain size (D) or larger interfacial resistance. Simultaneously, the correlation of κ_L to sound velocity varies from a cubic trend to a lower order as the phonon–boundary scattering of low-frequency phonons under room temperature no longer satisfies $\tau_{pp} = \tau_{total}$.

To separately account for the contribution from the strain-inhomogeneous-induced lattice softening effect and the boundary scattering in the HPT samples, herein, the experimental result of 0 and 1/2 rotations are plotted in Fig. 4 (a). Evidently, both the reduction in the phonon group velocity and the increase in the thermal resistance term γ contribute to low κ_L . The phonon MFP of corresponding cases is summarized in Fig. S9. Moreover, owing to the difference in the fundamental mechanism of the phonon boundary scattering and the lattice softening, the relative contribution can be identified from the temperature-dependent κ_L . As the decrease in phonon group velocity is identical under all temperatures, whereas phonon scattering is temperature-dependent, a smaller slope ratio of the normalized κ_L to temperature indicates lattice softening the dominant effect, whereas a larger slope ratio indicates the phonon scattering a more significant role⁴³. The results shown in Figure S3 suggest that boundary scattering played a critical role in the temperature range of 300–600 K for all HPT samples. Moreover, the decrease in slope ratio in cases of higher rotation suggests the enhancement of relative contribution from the lattice softening effect.

To explore the mechanism behind the enhanced interfacial thermal resistance due to HPT processing, a theoretical analysis was conducted using atomistic Green's function calculation (AGF) calculation (details in SI: Methods). The interatomic interaction was varied to adjust the lattice stiffness from approximately 12 to 167 GPa (no strain) and the interfacial thickness was varied to simulate the experimentally observed interfacial structure variation. Evidently, the interfacial thermal resistance increased with the softening of the interfacial layer (Fig. 4 (b)). Conversely, the thickness of the interfacial layer had a negligible impact on the interfacial thermal transport (Fig. S4). As the γ of the 1/2 and 0 rotation samples were given by the thermal conductivity calculation above (Fig. 4(a)), by plotting these values on the γ to Young's modulus curve in Fig. 4(b), we

obtained the corresponding Young's modulus and interfacial thermal resistance. The Young's modulus for 0 and 1/2 rotation samples are 35 GPa and 18 GPa, respectively, while their corresponding interfacial thermal resistance are 5.7 m²-K/GW and 14 m²-K/GW, respectively. With the gradual softening of the interfacial layer, the phonon transmission results suggest a decline in the overall frequency regime and a preferential suppression of phonon transmission at high frequencies. Herein, as the size effect of the nanostructure preferentially suppresses the κ_L of low-frequency phonons and interfacial softening predominately inhibits phonon transmission of high-frequency phonons, extreme suppression of thermal transport over the entire frequency range can be achieved, thus resulting in ultra-low κ_L in the HPT processed silicon.

Conclusions

In this study, the HPT process with relatively low pressure and torsion was employed to reduce the κ_L of nanocrystal bulk silicon. An ultra-low κ_L of 1.49 W/m-K, which is a remarkable value for near-100 % dense bulk-scale silicon, was achieved. Systematic structural characterization enabled understanding structural evolution during the HPT process clearly. A decrease in grain size, reorientation of the crystal, and generation of inhomogeneous strain inside the grain and at the interface were observed. The theoretical analysis revealed that the pronounced softening of the interfacial layer can effectively reduce interfacial phonon transmission. Additionally, the lattice softening of the overall structure can suppress the phonon group velocity and is essential for the eventual significant suppression of the κ_L (Fig. 4 (d)). From a physics perspective, this study provides valuable insights into the physics behind stress-induced phonon engineering, essentially shedding light on the underlying mechanisms for obtaining ultra-low κ_L . Furthermore, our findings suggest that the HPT process, with its cost-effectiveness and versatility, holds significant promise for reducing the κ_L of various bulk-scale materials.

Author Contributions

Bin Xu: Validation, Methodology, Formal analysis, Investigation, Writing - Original Draft. Yuxuan Liao: Software, Writing - Original Draft. Zhenglong Fang: Investigation, Validation. Yifei Li: Software. Rulei Guo: Methodology. Ryohei Nagahiro: Methodology. Yoshifumi Ikoma: Methodology, Writing - Review & Editing. Masamichi Kohno: Investigation. Junichiro Shiomi: Project administration, Funding acquisition, Writing - Review & Editing, Conceptualization, Visualization.

Conflicts of interest

The authors declare no conflict of interest.

Acknowledgements

This research was funded in part by JSPS KAKENHI (Grant No. 18H01384, 22K14189), JST CREST (Grant No. JPMJCR20Q3).

References

- 1 D. Ginting, C. C. Lin, L. Rathnam, J. H. Yun, B. K. Yu, S. J. Kim and J. S. Rhyee, *J. Mater. Chem. A*, 2017, **5**, 13535–13543.
- 2 F. Azough, A. Gholinia, D. T. Alvarez-Ruiz, E. Duran, D. M. Kepaptsoglou, A. S. Eggeman, Q. M. Ramasse and R. Freer, *ACS Appl. Mater. Interfaces*, 2019, **11**, 32833–32843.
- 3 J. L. Braun, C. H. Baker, A. Giri, M. Elahi, K. Artyushkova, T. E. Beechem, P. M. Norris, Z. C. Leseman, J. T. Gaskins and P. E. Hopkins, *Phys. Rev. B*, 2016, **93**, 140201.
- 4 K. Biswas, J. He, I. D. Blum, C. I. Wu, T. P. Hogan, D. N. Seidman, V. P. Dravid and M. G. Kanatzidis, *Nature*, 2012, **489**, 414–418.
- 5 J. Ravichandran, A. K. Yadav, R. Cheaito, P. B. Rossen, A. Soukiassian, S. J. Suresha, J. C. Duda, B. M. Foley, C. H. Lee, Y. Zhu, A. W. Lichtenberger, J. E. Moore, D. A. Muller, D. G. Schlom, P. E. Hopkins, A. Majumdar, R. Ramesh and M. A. Zurbuchen, *Nat. Mater.*, 2014, **13**, 168–172.
- 6 G. Chen, *J. Heat Transfer*, 1999, **121**, 945–953.
- 7 R. Hu, S. Iwamoto, L. Feng, S. Ju, S. Hu, M. Ohnishi, N. Nagai, K. Hirakawa and J. Shiomi, *Phys. Rev. X*, 2020, **10**, 21050.
- 8 M. N. Luckyanova, J. Mendoza, H. Lu, B. Song, S. Huang, J. Zhou, M. Li, Y. Dong, H. Zhou, J. Garlow, L. Wu, B. J. Kirby, A. J. Grutter, A. A. Puzos, Y. Zhu, M. S. Dresselhaus, A. Gossard and G. Chen, *Sci. Adv.*, DOI:10.1126/sciadv.aat9460.
- 9 J. Maire, R. Anufriev, R. Yanagisawa, A. Ramiere, S. Volz and M. Nomura, *Sci. Adv.*, 2017, **3**, 1–7.
- 10 S. Hu, S. Ju, C. Shao, J. Guo, B. Xu, M. Ohnishi and J. Shiomi, *Mater. Today Phys.*, 2021, **16**, 100324.
- 11 M. Christensen, A. B. Abrahamsen, N. B. Christensen, F. Juranyi, N. H. Andersen, K. Lefmann, J. Andreasson, C. R. H. Bahl and B. B. Iversen, *Nat. Mater.*, 2008, **7**, 811–815.
- 12 B. C. Sales, D. Mandrus and R. K. Williams, *Science (80-.)*, 1996, **272**, 1325–1328.
- 13 M. Arrigoni, J. Carrete, N. Mingo and G. K. H. Madsen, *Phys. Rev. B*, 2018, **98**, 115205.
- 14 T. Murakami, T. Shiga, T. Hori, K. Esfarjani and J. Shiomi, *Epl*, 2013, **102**, 46002.
- 15 B. Poudel, Q. Hao, Y. Ma, Y. Lan, A. Minnich, B. Yu, X. Yan, D. Wang, A. Muto, D. Vashaee, X. Chen, J. Liu, M. S. Dresselhaus, G. Chen and Z. Ren, *Science (80-.)*, 2008, **320**, 634–638.
- 16 A. Yamamoto, S. Ghodke, H. Miyazaki, M. Inukai, Y. Nishino, M. Matsunami and T. Takeuchi, *Jpn. J. Appl. Phys.*, DOI:10.7567/JJAP.55.020301.
- 17 K. T. Kim, S. Y. Choi, E. H. Shin, K. S. Moon, H. Y. Koo, G. G. Lee and G. H. Ha, *Carbon N. Y.*, 2013, **52**, 541–549.
- 18 J. Shiomi, *APL Mater.*, DOI:10.1063/1.4962935.
- 19 T. Claudio, N. Stein, D. G. Stroppa, B. Klobes, M. M. Koza, P. Kudejova, N. Petermann, H. Wiggers, G. Schierning and R. P. Hermann, *Phys. Chem. Chem. Phys.*, 2014, **16**, 25701–25709.

- 20 S. K. Bux, R. G. Blair, P. K. Gogna, H. Lee, G. Chen, M. S. Dresselhaus, R. B. Kaner and J. P. Fleurial, *Adv. Funct. Mater.*, 2009, **19**, 2445–2452.
- 21 A. Miura, S. Zhou, T. Nozaki and J. Shiomi, *ACS Appl. Mater. Interfaces*, 2015, **7**, 13484–13489.
- 22 V. Kessler, D. Gautam, T. Hülser, M. Spree, R. Theissmann, M. Winterer, H. Wiggers, G. Schierning and R. Schmechel, *Adv. Eng. Mater.*, 2013, **15**, 379–385.
- 23 G. Schierning, R. Theissmann, N. Stein, N. Petermann, A. Becker, M. Engenhorst, V. Kessler, M. Geller, A. Beckel, H. Wiggers and R. Schmechel, *J. Appl. Phys.*, , DOI:10.1063/1.3658021.
- 24 Y. Ikoma, *Mater. Trans.*, 2019, **60**, 1168–1176.
- 25 Y. Ikoma, K. Kumano, K. Edalati, K. Saito, Q. Guo and Z. Horita, *Philos. Mag. Lett.*, 2017, **97**, 27–34.
- 26 Y. Fukushima, Y. Ikoma, K. Edalati, B. Chon, D. J. Smith and Z. Horita, *Mater. Charact.*, 2017, **129**, 163–168.
- 27 S. Harish, M. Tabara, Y. Ikoma, Z. Horita, Y. Takata, D. G. Cahill and M. Kohno, *Nanoscale Res. Lett.*, 2014, **9**, 1–5.
- 28 C. Shao, K. Matsuda, S. Ju, Y. Ikoma, M. Kohno and J. Shiomi, *J. Appl. Phys.*, , DOI:10.1063/5.0037775.
- 29 Y. Ikoma, K. Matsuda, K. Yoshida, M. Takaira and M. Kohno, *J. Appl. Phys.*, 2022, **132**, 215101.
- 30 T. Kodama, M. Ohnishi, W. Park, T. Shiga, J. Park, T. Shimada, H. Shinohara, J. Shiomi and K. E. Goodson, *Nat. Mater.*, 2017, **16**, 892–897.
- 31 K. Biswas, J. He, Q. Zhang, G. Wang, C. Uher, V. P. Dravid and M. G. Kanatzidis, *Nat. Chem.*, 2011, **3**, 160–166.
- 32 X. Li, K. Maute, M. L. Dunn and R. Yang, *Phys. Rev. B - Condens. Matter Mater. Phys.*, 2010, **81**, 1–11.
- 33 K. Takahashi, M. Fujikane, Y. Liao, M. Kashiwagi, T. Kawasaki, N. Tambo, S. Ju, Y. Naito and J. Shiomi, *Nano Energy*, 2020, **71**, 104581.
- 34 Y. Ikoma, K. Hayano, K. Edalati, K. Saito, Q. Guo and Z. Horita, *Appl. Phys. Lett.*, 2012, **101**, 121908.
- 35 M. Kashiwagi, Y. Liao, S. Ju, A. Miura, S. Konishi, T. Shiga, T. Kodama and J. Shiomi, *ACS Appl. Energy Mater.*, 2019, **2**, 7083–7091.
- 36 R. Hanus, M. T. Agne, A. J. E. Rettie, Z. Chen, G. Tan, D. Y. Chung, M. G. Kanatzidis, Y. Pei, P. W. Voorhees and G. J. Snyder, *Adv. Mater.*, 2019, **31**, 1900108.
- 37 N. Hayazawa, M. Motohashi, Y. Saito and S. Kawata, *Appl. Phys. Lett.*, 2005, **86**, 1–3.
- 38 I. De Wolf, *Semicond. Sci. Technol.*, 1996, **11**, 139–154.
- 39 C. M. Poffo, J. C. De Lima, S. M. Souza, D. M. Trichês, T. A. Grandi and R. S. De Biasi, *J. Raman Spectrosc.*, 2010, **41**, 1606–1609.
- 40 S. Veprek, F. A. Sarott and Z. Iqbal, *Phys. Rev. B*, 1987, **36**, 3344–3350.
- 41 Z. Wang, J. E. Alaniz, W. Jang, J. E. Garay and C. Dames, *Nano Lett.*, 2011, **11**, 2206–2213.
- 42 T. Hori, J. Shiomi and C. Dames, *Appl. Phys. Lett.*, 2015, **106**, 171901.
- 43 R. Hanus, M. T. Agne, A. J. E. Rettie, Z. Chen, G. Tan, D. Y. Chung, M. G. Kanatzidis, Y. Pei, P. W. Voorhees and G. J. Snyder, *Adv. Mater.*, 2019, **31**, 1–10.
- 44 B. Jugdersuren, B. T. Kearney, J. C. Culbertson, C. N. Chervin, M. B. Katz, R. M. Stroud and X. Liu, *Commun. Phys.*, 2021, **4**, 1–10.
- 45 D. A. Broido, M. Malorny, G. Birner, N. Mingo and D. A. Stewart, *Appl. Phys. Lett.*, 2007, **91**, 19–22.